M. Brank, R. A. Pitts, G. Simič, P. Lamalle, M. Kocan,
F. Koechl, Y. Gribov, V. Polli, L. Kos

Assessment of plasma power deposition on the ITER ICRH antennas

Assessment of plasma power deposition on the ITER ICRH antennas

M. Brank, R. A. Pitts, G. Simič, P. Lamalle, M. Kocan, F. Koechl, Y. Gribov, V. Polli, L. Kos

Assessment of plasma power deposition on the ITER ICRH antennas

M. Brank[a]*, R. A. Pitts[b], G. Simič[a], P. Lamalle[b], M. Kocan[b], F. Köchl[c], Y. Gribov [b], V. Polli[b], L. Kos[a]**

[a]*Faculty of Mechanical Engineering, University of Ljubljana, Aškerčeva 6, 1000 Ljubljana, Slovenia*
[b]*ITER Organisation, Route de Vinon-sur-Verdon – CS 90 046-13067 St. Paul Lez Durance, France*
[c]*CCFE, Culham Science Centre, Abingdon, OX14 3DB, United Kingdom*

*first author: matic.brank@lecad.fs.uni-lj.si
**corresponding author: leon.kos@lecad.fs.uni-lj.si

Abstract

Ion cyclotron resonance heating (ICRH) is one of the three additional heating schemes to be deployed on ITER. Its two antenna arrays, installed on the outboard midplane, will deliver 20 MW of RF power in the 40-55 MHz frequency range. The plasma-facing component of the antenna assembly is the Faraday screen, comprising beryllium (Be) tile armoured, actively cooled bars located only ~1 cm radially behind the innermost point of the shaped Be first wall panels (FWPs). As such they are in close proximity to the scrape-off layer (SOL) plasma and it is important to assess the maximum heat loads that the screen bars may experience during high power ITER operation. This paper provides a detailed assessment of these loads using the new 3D field line tracing and power deposition framework SMITER [1]. The focus is on the H-mode, burning plasma scenario, taking into account both plasma thermal loading (including average loading due to mitigated Type I ELMs) and the loads due to photonic impact (assessed with the optical ray-tracing package Raysect [2]) from power radiated in the core obtained from integrated JINTRAC simulations. Calculations are also performed to assess the minimum allowed antenna to magnetic separatrix distances, for cases in which closer approach may be required to improve RF coupling.

1. Introduction

Ion cyclotron resonance heating (ICRH) is one out of three heating systems that will be deployed on the ITER tokamak. Its two antenna arrays, installed in port plugs on the outboard midplane (see Fig. 1a), will deliver 20 MW of radio-frequency (RF) power in the 40-55 MHz frequency range. The plasma-facing component of the antenna assembly is the Faraday screen (Fig. 1a), which has the dual purpose of polarizing the emitted RF radiation and protecting the electrically active components of the arrays from direct plasma contact.

The Faraday screens comprise beryllium (Be) tile armoured, actively cooled bars - denoted here as Faraday Screen Bars (FSB) - and are located nominally ~10 mm radially behind the innermost point of the shaped Be first wall panels (FWPs) mounted on the main neutron shielding blanket. As such they are in close proximity to the scrape-off layer (SOL) plasma and it is important to assess the maximum surface heat loads that the screen bars may experience during ITER operation. This paper provides such an assessment, with primary focus on the Q = 10 burning plasma scenario which is expected to provide the most severe stationary loading conditions. Additional contributors (RF skin losses and, in fusion plasmas, volumetric neutron heating) must also be included to compute the final thermal load on screen components but are out of the scope of this study.

Non-negligible plasma loads may also be expected in the case of an L-mode or ohmic outboard limiter plasma, a configuration which cannot be excluded, particularly in current ramp-down phases of ITER discharges, but which would not be deliberately performed under stationary conditions at any significant power level. Analysis similar to that described in detail here for the high performance diverted plasmas has been been performed but is not reported here for brevity. The maximum estimated limiter heat loads are comparable, but lower than the worst case values found for the burning plasma.

Plasma-induced heat loads to the FSBs, and indeed to all the FWPs, are comprised of contributions from charged particle impact and from photonic/charge-exchange neutral (CXN) bombardment. The former are deposited by charged particles constrained to follow magnetic field lines, whilst the latter is independent of the field and can be considered as a quasi-perpendicular load. It is only in the case of the burning plasma that these more uniform perpendicular loads will make any serious contribution to the loading profile. In fact, as will be shown in Section 3, for the "baseline" burning plasma (diverted) equilibrium, the distance between the outer midplane separatrix and the outer wall is sufficiently large that there will be no thermal plasma load at all on the antenna screen bars due to their recess behind the first wall radius. This is not, of course, the case for outboard limiter plasmas, for which the last closed magnetic surface (LCFS) is in contact with the FWPs.
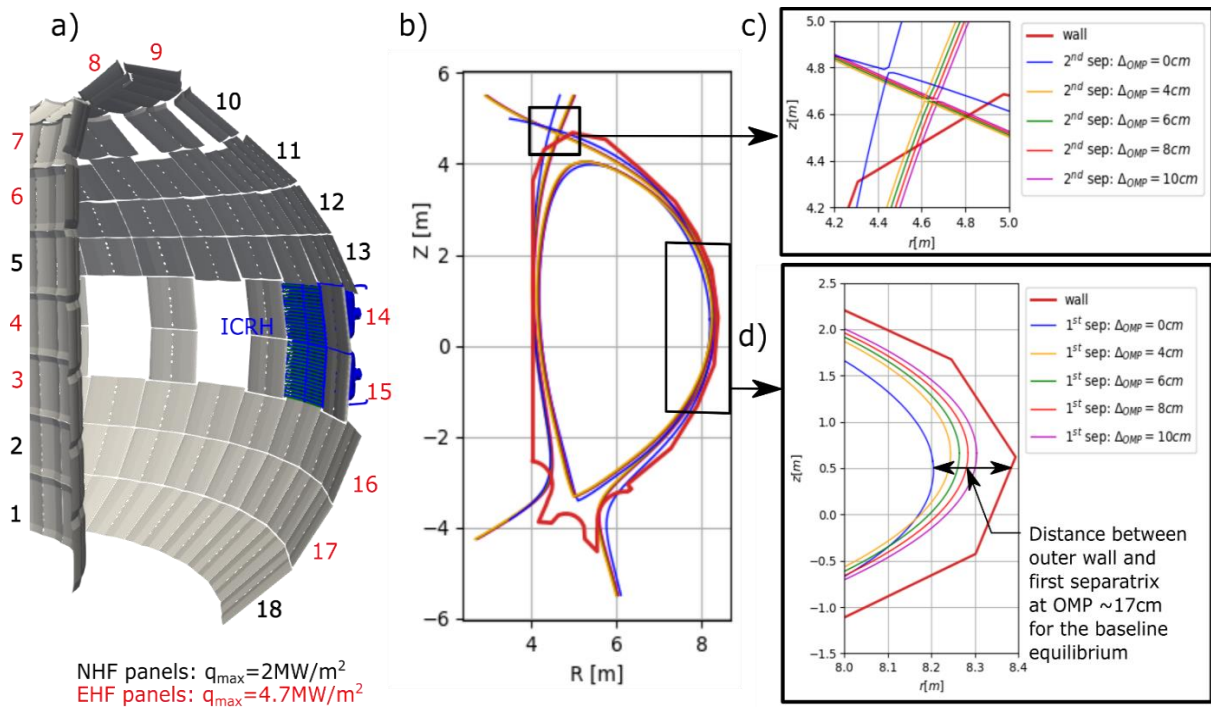
Figure 1: a) Portion of the 3D in-vessel component model used in the SMITER code to perform the field line tracing, featuring a simplified description of the shaped FWPs and including one of the two ICRH antenna front ends (in blue). The FWP panel numbering is included, distinguishing the Normal (NHF) and Enhanced (EHF) variants (numbered in red) according to their stationary power handling capacity. b) Baseline burning plasma magnetic equilibrium together with the family of additional equilibria studied here with progressively increased radial shift of the outer midplane (OMP) separatrix and second separatrix ($\Delta_{OMP} = 4, 6, 8, 10\ cm$). c) Close-up in the vicinity of FWP #8, showing the intersection of the second separatrix (see also Section 3.1) d) Close-up in the vicinity of the ICRH antenna illustrating more clearly the shifted equilibrium positions (note that the aspect ratio has been adjusted for visualization purposes).

An important question addressed here, is how the antenna thermal loading increases when the outer separatrix is moved closer to the antenna. The coupling of power in the ion cyclotron frequency range is critically dependent on the SOL density (the fast wave is evanescent below its cut-off density). Depending on the shape of the SOL density profile, one option if coupling of the RF power turns out to be insufficient in the baseline configuration, is to move the separatrix closer to the antenna (another is localized gas injection near the antennas [3]). Figure 1b illustrates this for the ITER burning plasma equilibrium, in which slight modifications to the scenario design (using the DINA code) have been used to place the outboard separatrix progressively closer to the wall.

As the wall is approached, the 3D geometry of the system will begin to allow some field line penetration into the port plug recess so that plasma thermal loading can occur on the antenna front end structures. This can only be assessed with field line tracing in the full 3D environment of the first wall (Fig. 1a), together with a model for the SOL parallel heat fluxes flowing along these field lines. Such an assessment is performed here using the new 3D field line tracing and power deposition framework SMITER [1]. In practice, as this paper will show, the allowable separatrix displacement is fixed not only by loading on the antenna structures, but by heat flux to the FWPs. Regarding the photonic power loading, this is examined here using the Raysect optical ray-tracing package [2], together with integrated modelling predictions for the core plasma radiation under burning plasma conditions (Section 2.4).

2. Input power load and specifications

As mentioned in Section 1, the two main components of the antenna (and indeed the whole first wall) loading, are the thermal plasma (Sections 2.1-2.3) and the radiative/CXN fluxes (Section 2.4). The latter, for the first wall, originate mostly from the core plasma and, unlike the thermal plasma loads, do not follow magnetic field lines. For the analysis here, which focusses on the burning plasma, the SOL heat fluxes flowing parallel to field lines are assumed to comprise a stationary component and a contribution from (mitigated) Edge Localized Modes (ELMs) [4]. Together, these components exhaust the power flowing into the SOL in the baseline burning plasma (~100 MW). Although ITER aims to try and suppress ELMs [5], it is assumed here for conservatism with regard to antenna loads, that only mitigation is achieved, at a level consistent with tolerable divertor target transient power loading and sufficiently low ELM-induced tungsten (W) contamination of the pedestal plasma (due to divertor target sputtering).

The input specifications for the ICRH antenna load calculations for each of these three contributions (thermal plasma ELM and inter-ELM and photonic radiation) are briefly described in the following sub-sections. For the stationary (inter-ELM) and ELM parallel fluxes, the specification is essentially identical to that described in [4], though the more complex magnetic field line connection profile in the far SOL region occupied by the ICRH antenna means that the simpler analytic approximation used to determine the ELM heat flux in [6,7] cannot be used.

The thermal plasma loads described here are loads *parallel* to the magnetic field. To obtain the resulting heat fluxes on real surfaces, they must be projected onto those surfaces, taking into account the full 3D geometry. This is one of the main functions of the SMITER code. The results of this projection will be presented in Section 3.

2.1. Stationary (inter-ELM) profile

In terms of the worst case first wall heat loading to be expected, the ITER burning plasma specification for inter-ELM loads [4] assumes a broad "density shoulder" in the SOL, seen on many present devices when operating at high density under detached divertor conditions. Unfortunately, the situation still remains uncertain, with different devices observing broadening under different conditions in H-mode plasmas.

The physics basis for the broadening is predicated on strong radial filamentary ("blobby") turbulent convective transport of particles, leading to high wall fluxes. However, it is still not possible to provide quantitative predictions for ITER and so the specification in [4] is adopted here: a double exponential parallel heat flux profile with a sharp near-SOL feature with characteristic width, $\lambda_{qn} \sim 0.005\ m$, followed by a broad "shoulder" in the far SOL with $\lambda_{qf} \sim 0.017\ m$. The breakpoint is fixed, somewhat arbitrarily, at a distance of $R_b = 0.0025$ m from the primary separatrix, well into the main SOL where field lines connect the inner and outer divertor targets. This has been the specification adopted for the power handling design of the FWPs and gives a conservative upper limit in which ~20% of the SOL thermal plasma power is deposited on the main chamber wall. Note that the radial separation between the primary and secondary separatrices in the baseline equilibrium is $\Delta_{r,sep} \sim 0.09\ m$.

Assuming simple 0D power balance, the resulting parallel heat flux radial profile, $q_{\parallel s}(r)$ provided as input to the SMITER field line tracing code may thus be written:

$$
q_{\parallel,s}(r) = \begin{cases} \dfrac{FP_{sol}B_{\varphi,OMP}}{2\pi R_{OMP}B_{\theta,OMP}\lambda_{qn}} \exp\left(-\dfrac{\triangle r}{\lambda_{qn}}\right); & \text{for } \triangle r < R_b \\[4mm] \dfrac{FP_{sol}B_{\varphi,OMP}}{2\pi R_{OMP}B_{\theta,OMP}\lambda_{qn}} \exp\left(-\dfrac{\triangle r}{\lambda_{qf}} + \dfrac{R_b}{\lambda_{qf}} - \dfrac{R_b}{\lambda_{qn}}\right); & \text{for } \triangle r > R_b \end{cases}
\tag{1}
$$

With $B_{\varphi,OMP}, B_{\theta,OMP}, R_{OMP}$ the toroidal and poloidal fields and major radius at the OMP. Parameter $F = 0.5$ sets equal power flows to inner and outer targets.

2.2. ELM profile

To prescribe an average ELM wall heat flux, the ELM filament parallel loss model (PLM) in [6,7] is adopted. Each ELM is assumed to comprise a number, n_{fil} of equal filaments which are launched from the primary separatrix (so that the initial energy per filament, $W_{fil0} = \Delta W_{ELM}/n_{fil}$ for given ELM energy loss from the confined plasma, ΔW_{ELM}) and propagate across the main chamber SOL with a specified velocity. Following [7], the filament energy balance may be written:

$$
q_{\parallel,fil}\left(\Delta r_{sep}, z, t\right) = -\frac{dW_{fil}}{dt}\frac{1}{4\pi\sigma_r\sigma_z} e^{-\frac{(\Delta r_{sep} - tv_r)^2}{2\sigma_r^2}} e^{-\frac{\Delta z^2}{2\sigma_z^2}}
\tag{2}
$$

where W_{fil} and v_r are the filament energy and radial speed respectively, with the filament energy loss rate due to parallel transport, dW_{fil}/dt computed using the fluid model described in [8]. The filament structure in the poloidal (R-z) plane is approximated by a Gaussian profile with half-widths σ_r and σ_z (see Fig. 2 in [7]), with values $\sigma_r = 3$ cm and $\sigma_z = 45$ cm (at the OMP) chosen as in [7] and inspired by non-linear MHD simulations of mitigated ELMs on

ITER with the JOREK code [9]. The filament vertical height at the OMP ($2\sigma_z$) is fixed such that the filament gap-to-size ratio $r_{gapfil} = \pi R_{omp}(B_\theta/B_\varphi)_{omp}/n_{fil}\sigma_z \sim 2$, also consistent with JOREK simulations.

A key input to the parallel energy loss computation is the magnetic connection length, L_{conn} along the filament flux tube from the OMP to the solid surfaces at each end of the tube. The OMP radial profile of L_{conn} is computed using SMITER (see Section 2.3) and shows a complex structure in the far-SOL, beyond the second separatrix, where field lines no longer connect from inner to outer divertor target, but are instead delimited by much shorter distances between outboard FWPs. Since the ICRH antenna, on which the power loads are required, is located in this far SOL region, the analytic solution to Eq. (2) derived in [7] assuming an approximately constant λ_q, cannot be employed here and Eq. (2) must be solved numerically to obtain the ELM filament parallel energy density, $E_{\|,fil}(r)$, at any point in the OMP radial profile. From this, the quantity of importance for engineering studies, the average ELM parallel heat flux, may be simply obtained as

$$\langle q_\| \rangle_{ELM}(r) = \frac{E_{\|,fil}(r)f_{ELM}}{2} \tag{3}$$

with f_{ELM} the ELM frequency, determined by the requirement that Type I ELMs exhaust a fraction of P_{SOL} in the range $P_{ELM} = f_{ELM}\Delta W_{ELM} = (0.2 - 0.4)P_{SOL}$ [4]. The factor 2 in Eq. (3) originates from the assumption $r_{gapfil} = 2$, namely that a heat flux of magnitude corresponding to that in the centre of each filament flows through half of the OMP toroidal circumference. It is equivalent to the case in which ELM filaments, launched from random toroidal locations, strike given FWP locations on average at every second ELM.

Given fixed magnetic geometry (i.e. magnetic equilibrium) and fixed ELM filament geometry and plasma assumptions (filaments are launched from the primary separatrix with half the pedestal top values of density and temperatures for the burning plasma baseline ($T_{i,ped} = T_{e,ped}$=5 keV, $n_{e,ped} = 7.5 \cdot 10^{19}\ m^{-3}$, as in [6,7])), the only free parameters in the averaged ELM heat flux calculation are v_r and f_{ELM}. Here, analysis is restricted to just one particular example case ($f_{ELM} = 33\ Hz, \Delta W_{ELM} = 0.6\ MJ$) consistent with the choices in [6,7], which are themselves consistent with the requirements for tolerable ELM transient divertor heat loads (W monoblock surface melting) and core W accumulation [10].

2.3. Mapping the thermal plasma loads

To compute surface heat loads due to the ELM and inter-ELM thermal plasma components described in Sections 2.1 and 2.2, the radial profiles of parallel heat flow need to be mapped onto the first wall and ICRH antenna structures. This is performed here using the field line tracing software SMITER [1], taking into account the full 3D geometry of the first wall and ICRH antenna. The code is also used to extract the connection lengths (Fig. 2) which are a key input parameter to the PLM for the calculation of the ELM filament energy exhaust along the magnetic field. An important point to note in connection with the field line tracing is that 3D perturbation of the magnetic field lines, in particular due to the magnetic perturbations induced by the ELM control coils, are not taken into account in the analysis here.

Field lines are traced from all FWP/antenna mesh points within a 20° toroidal sector encompassing the antenna and its neighbouring FWPs at 40 equally spaced toroidal positions inside this sector. Connection lengths can be computed in two directions: from the OMP

towards the inner (Fig. 2a) and outer (Fig. 2b) targets. In the vicinity of the outboard FWPs and the ICRH antenna the connection lengths vary toroidally due to the 3-D geometry, such as the FWP toroidal shaping and the recessed area of the midplane port in which the antenna is housed. This effect can be seen in Fig. 2b for $\Delta_{OMP} = 4cm$, where the profiles of L_{conn} for each toroidal location begin to differ (marked with cyan colour) as the apex position of FWP #15 is approached.
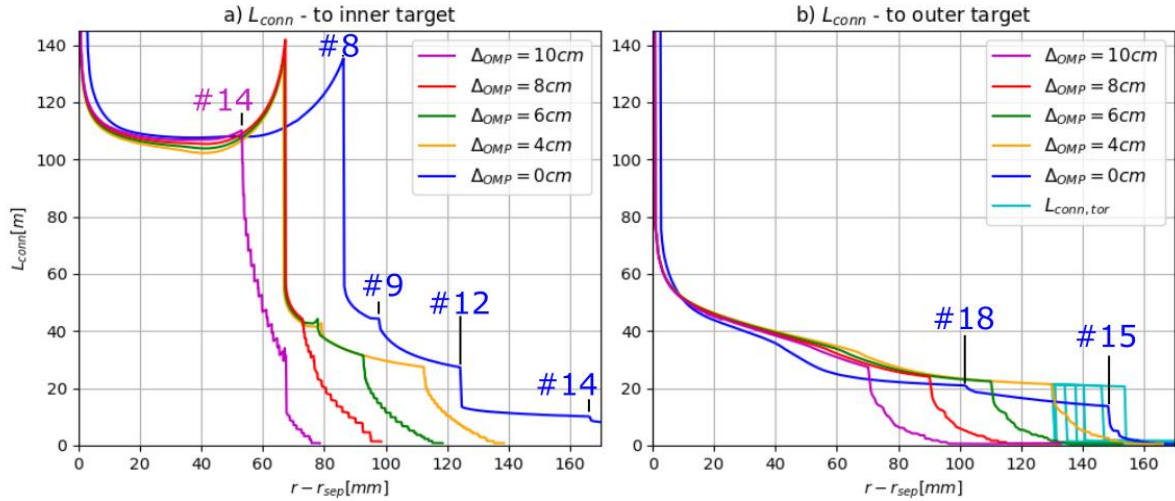
Figure 2: (a) Connection length profiles starting from the OMP towards (a) the inner target and (b) the outer target for the baseline burning plasma equilibrium ($\Delta_{OMP} = 0\ cm$) and the 4 shifted equilibria shown in Fig. 1(b, d). The radial locations of the intersection with various FWPs (Fig. 1a) are labelled. The shortest of the connection lengths (namely those to the outer divertor target) are used as input to the ELM parallel loss model.
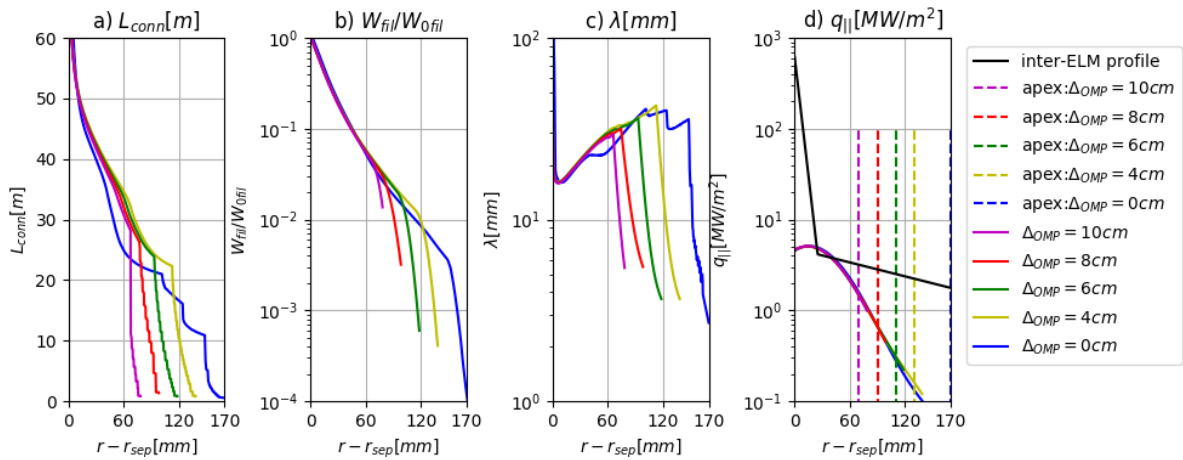
Figure 3: Compilation of results of the ELM PLM for the set of equilibria with $\Delta_{OMP} = 0, 4, 6, 8$ and $10\,cm$. (a) OMP to outer target connection lengths repeated from Fig. 2b but on a more compressed y-axis scale (b) ELM filament energy normalized to the inital energy (c) filament energy decay length (d) maximum ELM-averaged heat flux (assuming $v_r = 500\,ms^{-1}, \Delta W_{ELM} = 0.6\,MJ, n_{fil} = 10$ and $f_{ELM} = 33\,Hz$ – see text) plotted together with the stationary (inter-ELM) profile for $P_{SOL} = 100\,MW$. Radial locations of the apex of FWP #15 at the OMP are marked by the vertical dashed lines. All parameters are graphed against the distance from the primary separatrix at the OMP.

The connection length profiles also of course naturally change as the equilibrium is shifted towards the outer wall. In Fig. 2a, giving $L_{conn}(r)$ from the OMP to the inner target, the location of the secondary separatrix can clearly be seen as the point at which the connection length begins to rise, corresponding to the approach to the secondary X-point. Thereafter, the far SOL region is accessed and field line connections are made between two locations on the outboard wall rather than between the two divertor targets. As a result, the values of L_{conn} fall rapidly and the profile has a disjointed structure as the various outboard FWPs are intercepted (see FWP number labels in Fig. 2). The shortest lengths correspond to field lines connecting with FWPs #14, 15, the direct neighbours of the ICRH antenna. For input to the ELM PLM, the shortest connection lengths from OMP to the outer target (Fig. 2b) are used since this represents the fastest sink of parallel energy ($\tau_{\parallel} \, \mu \, L_{conn}/c_s$ with c_s the ion sound speed) to the target and will always dominate the rate at which ELM filament energy is dissipated as the filaments transit across the SOL from the assumed OMP launch point.

The outputs of the PLM for the radial OMP-outer target connection length profiles in Fig. 2b are shown in Fig. 3. The ELM filament energy, normalized to the initial filament energy, decreases steadily with increasing radial distance, with a transition to a faster rate of decrease once L_{conn} drops in the far SOL region. Here, the initial filament energy, W_{fil0} is fixed assuming $\Delta W_{ELM} = 0.6\,MJ$ and $n_{fil} = 10$, corresponding to typical mode numbers for Type I ELMs and with an energy loss per ELM approximately consistent with tolerable divertor target transient loads [10]. At these values of ΔW_{ELM}, ELM frequencies in the range of a few tens of Hz are expected to be acceptable from the point of view of tungsten (W) accumulation in the pedestal due to ELM-induced W sputtering at the divertor targets (see also [10]).

As shown by Eq. 2, the temporal and radial evolution of W_{fil} and $q_{\parallel}$ can be related through velocity of the filament v_r, which determines the fraction of W_{fil} remaining at FW contact and thus the ELM first wall loading. Experimentally measured values of v_r are scarce and vary widely in the range of a few $100\,m/s$ up to a few km/s [8]. The analysis in this paper assumes a baseline value of $v_r = 500\,m/s$.

The local decay length of the filament energy obtained through the PLM is shown in Fig. 3c, with the average parallel ELM energy density profile from Eq. 3 plotted in Fig. 3d, together, for comparison, with the assumed, "worst case" inter-ELM stationary heat flux profile specified in Section 2.1 for $P_{SOL} \sim 100\,MW$ (see Eq. 1). Evidently, this rather conservative specification for the inter-ELM heat flux means that only for the largest separatrix shifts would the ELM energy deposition even begin to be comparable to the inter-ELM loading (see Section 3).

One caveat with the relatively crude analysis described here is that the ELM and inter-ELM heat fluxes are not self-consistent in the sense that the total power convected to the walls by the two contributions are computed completely separately. Thus, for the example in Fig. 3d, the average ELM power ($\Delta W_{ELM} f_{ELM} \sim 20\,MW$) is to be added to that exhausted by the inter-ELM power, for which $P_{SOL} = 100\,MW$ is assumed in Eq. 1. Integration across the SOL of the two

separate profiles in Fig. 3d does in fact retrieve, to within $\sim 2\%$, the total injected power of $\sim 120\ MW$.

The perpendicular power flux density onto the PFCs, $q_{\perp,PFC}$ is given by

$$q_{\perp,PFC} = \frac{R_{OMP}}{R_{PFC}} q_{||}(\Delta r) \sin \alpha \qquad (4)$$

where, R_{PFC} is the major radius at the point of the calculation of power deposition, Δr is the radial distance in the SOL to the point of intersection, α is the total angle between the PFC and the incident field lines and $q_{||}$ is the sum of the ELM averaged and inter-ELM heat fluxes.

2.4. Photonic radiative power

To provide a realistic assessment of the photonic power loads to be expected on the ICRH antenna front end, the optical ray-tracing package Raysect [2] is used in conjunction with simulations of the core radiated power from integrated core-edge modelling of ITER burning plasma scenarios performed with the JINTRAC suite of codes [11]. These modelled scenarios are stored in the ITER Integrated Modelling Analysis Suite (IMAS) and any given output field can be easily recalled for implementation in subsequent post-processing. In the case of the antenna photon loading estimates, the important quantity is the core distribution of total radiated power from all sources (e.g. line, Bremsstrahlung and synchrotron radiation). Since JINTRAC is a 2D code, but the full 3D antenna photon loading is required, the radiation profile is given as a structured grid on which each element is characterized by a rectangle and is assumed to be toroidally symmetric.

The two example distributions used here are shown in Fig. 4, each of which is for burning plasma at Q = 10. In both cases, W is the dominant core impurity and both correspond to a "worst case" (in terms of ICRH power loading) in which a very high W source is prescribed at the plasma boundary, leading to core radiation levels of ~50 MW, eventually provoking an H-L back transition (radiative collapse). An additional "rotation factor" [12]: $\exp(M^*(\rho,\theta)/2)/\langle\exp(M^*(\rho,\theta)/2)\rangle$ has been applied to the radiation distribution (assuming all the radiation is due to W) to simulate the poloidal asymmetries arising in the W distribution due to corrections in the impurity neoclassical transport driven by the rotation.
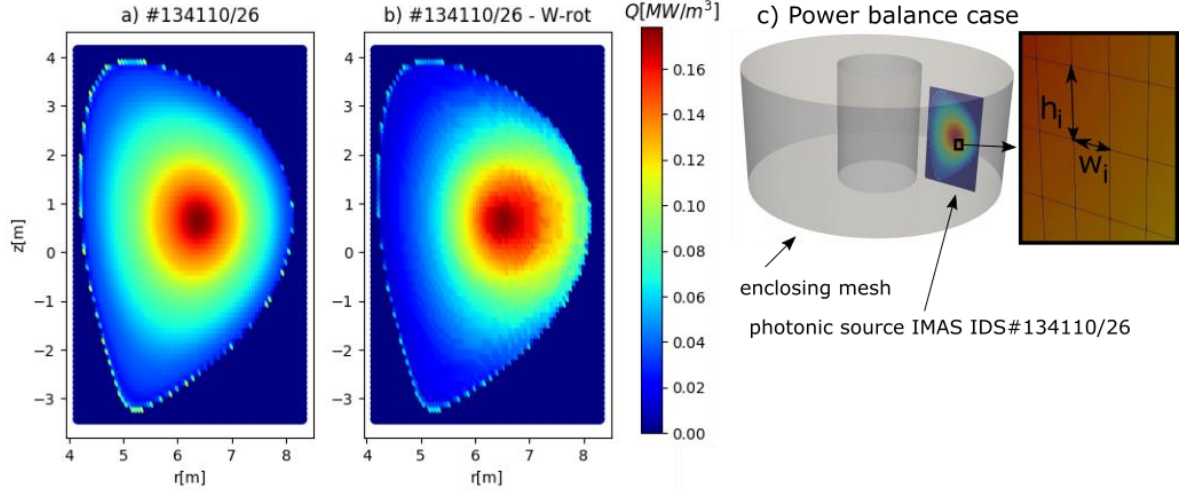
Figure 4: Distributions of core radiated power from JINTRAC core-edge simulations of the ITER burning plasma (Q = 10) baseline H-mode assuming W as the dominant impurity and including (a) "standard" and (b) artificially enhanced rotation factors on the radiation distribution. (c) Configuration for the Raysect power balance check.

Here, M^* is the rotation Mach number, given by $M^*(\rho, \theta) = m^* \Omega(\rho)^2 R(\rho, \theta)/T_i(\rho)$, where m^* is the effective impurity mass, Ω is the angular frequency of toroidal plasma rotation, $R(\rho, \theta)$ is the major radius, $T_i(\rho)$ is the ion temperature and ρ the radial coordinate across the plasma cross-section. In Fig. 4a, the rotation factor is computed on the basis of the standard angular rotation computed in JINTRAC, whilst in Fig. 4b the factor has been chosen to be at the upper limit of expectations for momentum transport in the ITER baseline scenario. Unlike the rather poloidally symmetric distribution in Fig. 4a, the much stronger rotation in Fig. 4b produces a skewed profile which should provide the worst case antenna photonic loading.

To calculate the incident photonic heat fluxes, Raysect projects a finite number of rays N_{ray} from every triangle of the mesh (generated in SMITER) used to describe the ICRH antenna and FWP surfaces. This mesh is called an observer. The path of every ray is then traced and if the ray does not intersect any light source (plasma), the contribution of this source to the total power on the triangle is set to 0. The governing equation of total power (radiant flux) on the surface is given by the integral of the incident radiance L over the collecting solid angle, Ω and surface, A:

$$P_i = \int_{A_i} \int_\Omega L_i(r, \omega) \cos\theta \, d\omega dA \qquad (5)$$

Here, P_i is the total power on the individual triangle. If the ray does intersect the plasma, the contribution to the total power is calculated through Monte-Carlo (MC) integration of the plasma source on the part of the path which travels through the plasma source. The statistical uncertainty of MC integration can be reduced by increasing N_{ray}. The statistics of this method is described in more detail in [13]. Once Raysect has evaluated P_i, the photonic power density can then be calculated through the area of any given triangle: $q_i = P_i/A_i$.

To save computational time, and benefitting from the toroidal symmetry of the radiation source, only one third of the tokamak is simulated, with mirrors implemented at each boundary so that rays are specularly reflected back into the simulation region (so no power of the ray is lost due

to reflection). The vertical plane of symmetry of the ICRH antenna and its near-symmetry in the horizontal plane, combined with its location (centred on the OMP) relative to the radiation source, allow further reductions in CPU time by setting only the upper right quadrant of the Faraday screen and straps as the observer for the radiation calculation. The surfaces of the FWPs and divertor are treated as fully absorbing, meaning that a given ray is terminated if it intersects the triangles of FWP and divertor meshes. This is a conservative assumption from the point of view of the deposited heat load on the antenna, but may slightly underestimate the incoming radiation due to the lack of reflections in the main chamber.

To check approximate power balance for the MC calculation, a toroidal mesh enclosing the radiative profile (Fig. 4c) is used to compute the total photonic power deposited onto this mesh, taken as observer. In the case of the JINTRAC simulation in Fig. 4a, this integration yields a total power of $56.3\ MW$, to be compared with the actual simulation value of $55.3\ MW$.

3. Results
3.1. Thermal loads

The distribution of power deposition due to plasma loads on the ICRH antenna for the series of equilibria with increasing different Δ_{OMP} (see Fig. 1b, c, d) are shown in Fig. 5. All cases are computed for the combination $\Delta W_{ELM} = 0.6\ MJ, f_{ELM} = 33\ Hz, v_r = 500\ ms^{-1}$ discussed in Section 2.3 for the ELMs and for the inter-ELM profile specification of Section 2.2. In the baseline scenario (thus $\Delta_{OMP} = 0\ cm$), the ICRH Faraday screen is completely shadowed by the neighbouring FWPs, so no field lines penetrate to the antenna screen and no plasma particle power is deposited.

With increasing Δ_{omp} magnetic field line penetration starts to occur and the wetted areas on the FSBs grow. As shown by the zoomed inserts in Fig. 5, for $\Delta_{OMP}\ £\ 6\ cm$ the peak power deposition actually appears on the vertical sides of the screen bars due to the higher field line impact angle (~20°) compared to the front surfaces (~3°). For the cases with $\Delta_{OMP} = 8$ and $10\ cm$, the peak loads (~$2\ MWm^{-2}$) move to the perpendicular extremities of the bars, striking the surface at very high angles (~70°). The peak values are compiled in Table 1 for the different FSB locations.

a) $q_\perp$: $\Delta_{OMP} = 4\ cm$ b) $q_\perp$: $\Delta_{OMP} = 6\ cm$ c) $q_\perp$: $\Delta_{OMP} = 8\ cm$ d) $q_\perp$: $\Delta_{OMP} = 10\ cm$

$q_{\perp,\max} \sim 0.76 MW/m^2$ $q_{\perp,\max} \sim 0.92 MW/m^2$ $q_{\perp,\max} \sim 2 MW/m^2$ $q_{\perp,\max} \sim 2.3 MW/m^2$

e)   f)   g)   h)

front face

poloidal face

i)

end face
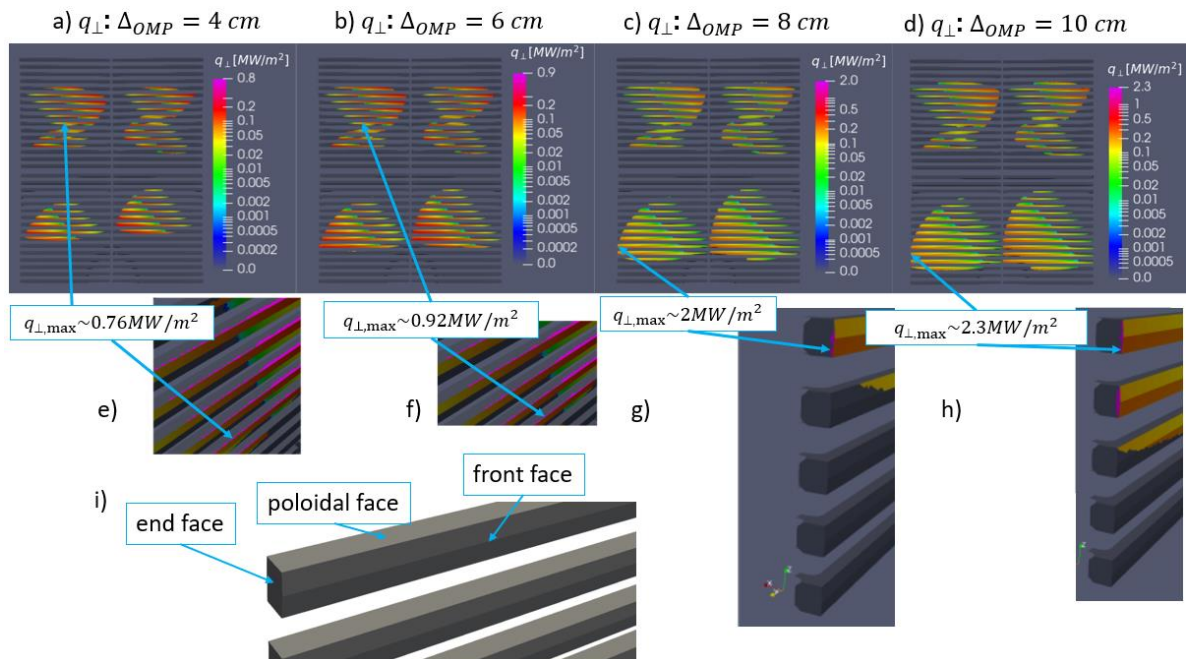
Figure 5: (a-d) Power deposition on the ICRH antenna FSBs for the 4 values of Δ_{omp} in Fig. 1b, d (the baseline, unshifted case is not shown because there is no wetted area). The zoomed regions in (e-h) indicate the locations of the peak power deposition given in Table 1. The geometry in (i) defines the terminology used in the main text for the individual PFC faces on the FSB

At the time of writing the antenna is entering the final design phase and the details of the Be clad FSB design have not been finalized. The present analysis thus provides a basis for the expected peak loads and an assessment of the maximum plasma displacement compatible with the Faraday screen design. This is important information for validation and assessment of the final antenna design, since its maximum performance will be a trade-off between antenna coupling and thermal power handling of the screen components.

Even if the estimated peak stationary FSB heat loads may be tolerable, it is also important to check the FWP loading across the whole outboard side of the machine as the separatrix is moved outwards toward the walls. This has also been completely traced within SMITER and the results are shown in Fig. 6 for the baseline equilibrium and the series of 4 shifted equilibria for FWPs #8-18. The highest power densities are found on FWPs #8, 9, 14, 15, 18, as would be expected: FWP #8, 9 and 18 correspond to the intersection of the secondary separatrix, whilst FWP #14, 15 span the outboard midplane location, which becomes heavily loaded when Δ_{OMP} becomes very large.
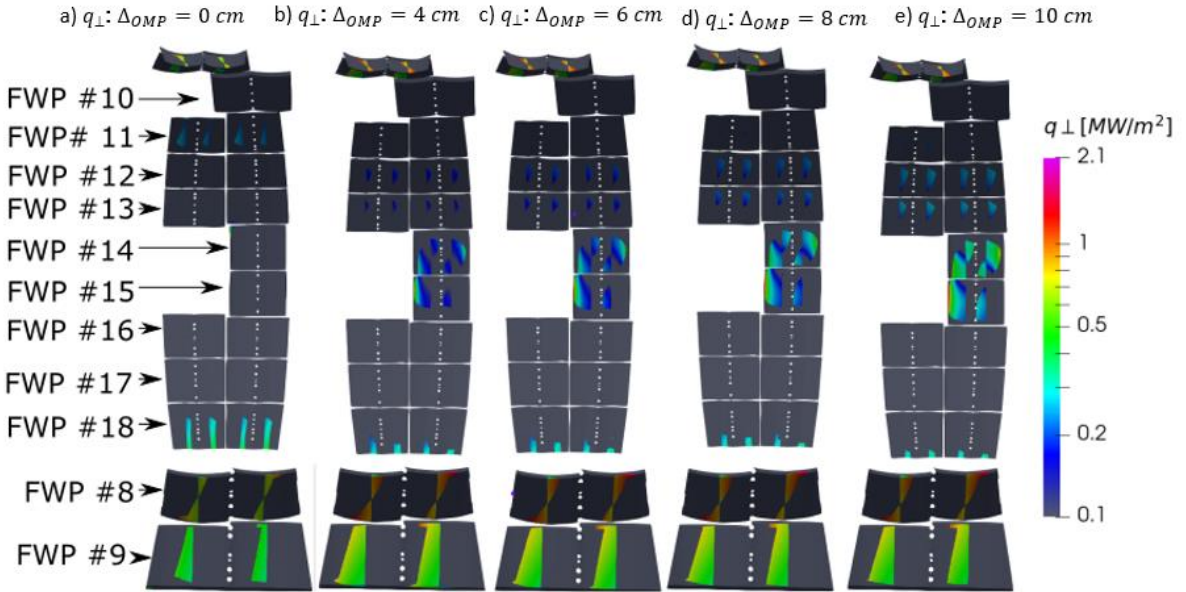
Figure 6: (b-e) Plasma thermal power loading on the outboard FWPs #8-18 as Δ_{OMP} increases from the baseline, non-shifted equilibrium in (a).

Δ_{OMP} [cm]	$q_{\perp max}$ [MW/m^2] FWP #8	$q_{\perp max}$ [MW/m^2] FWP #9	$q_{\perp max}$ [MW/m^2] FWP #14	$q_{\perp max}$ [MW/m^2] FWP #15	$q_{\perp max}$ [MW/m^2] FWP18	$q_{\perp max}$ [MW/m^2] FSB (front)	$q_{\perp max}$ [MW/m^2] FSB (side)	$q_{\perp max}$ [MW/m^2] FSB (end)
0	1.28	0.5	0	0	0.42	0	0	0
4	1.78	1.07	0.42	1.32	0.33	0.185	0.76	0

6	1.76	1.07	0.53	1.62	0.34	0.22	0.92	0
8	1.77	1.04	0.64	1.8	0.35	0.32	1.1	2
10	1.71	1.01	0.76	2.1	0.36	0.347	1.56	2.3

Table 1: Maximum computed power densities on FWPs #8, 9, 14, 15, 18 and ICRH FSBs (see Figs. 5 and 6) for the combined ELM and inter-ELM heat flux profile and all values of Δ_{OMP}.

The highest peak heat loads occur on FWPs #8 and 15, with $q_\perp \sim 2.0\ MWm^{-2}$ (see also Table 1). This is still well within the power handling capability ($\sim 4.7\ MWm^{-2}$) of these EHF panels

(see Fig. 1a), but to the values shown in Fig. 6 and Table 1 must be added penalty factors for panel misalignment, tilting, castellation etc. [14]. This can amount to as much as a factor 2 for the FWPs neighbouring the ICRH antenna so that for Δ_{OMP} ³ 8 cm in the series considered here, FWP loading might be expected to be marginal with respect to allowed limits, depending on the details of the far SOL stationary + average ELM heat fluxes. Note further that for the highest Δ_{OMP}, the wetted area increases on FWPs #14, 15 on either side of the antenna such that the peak power deposition starts to occur on the edges of the panels where impact angles are high. This is a situation to be avoided in practice because overload can quickly occur for small increases in $q_{||}$.

Regarding the heat loads on FWP #8, 9, where the secondary separatrix strikes the main wall, their values (Table 1) are relatively constant with increasing Δ_{OMP}. This is due to the approximately constant secondary separatrix strike point position (Fig. 1c) and constant distance between the first and second separatrix at the OMP throughout the Δ_{OMP} scan (for values of Δ_{OMP} > 0 cm). This is in fact deliberately arranged in the design of the shifted equilibria. The penalty factors (~50%) for these FWPs in the secondary X-point region are lower than for those neighbouring the ICRH antenna, so the power loading remains within acceptable levels even when $\Delta_{r,sep}$ reduces as Δ_{OMP} increases (see Fig. 2a).

3.2. Photonic loads

Using the methodology and plasma simulation cases described in Section 2.4, the calculated radiative power deposition on the ICRH antenna is shown in Fig. 7. Here, the worst case plasma in Fig. 4 is assumed, with deliberately enhanced W impurity rotation providing a poloidally asymmetric shift in the core radiation profile increasing photonic loads at the antenna location. There are three main ICRH antenna components which receive radiative power loading: the FSBs, the antenna housing module and the straps located behind the FSBs. Being closest to the plasma source, the FSBs receive the highest loads (peak value of ~0.12 MWm⁻²). The shield housing module receives the highest loads (~0.1 MWm⁻²) on the edges since they are the most exposed to the radiative source. The power deposition on the straps naturally features a striped pattern, since part of the area is shadowed by the FSBs. The maximum heat load on the exposed areas is 0.074 MWm⁻² for this particular loading case.

These peak stationary photon heat loads are about a factor 2 lower than the worst case stationary values given in the ITER Heat Load Specification [7]. This considers an even worse case, hypothetical core radiated power (of ~80 MW), corresponding to the maximum power that could in theory be radiated and still allow the burning plasma to remain in H-mode, together with a higher peaking factor than that associated with the poloidally asymmetric radiation distribution in Fig. 4. The loads assessed here are more typical of real conditions and properly take into account the full 3D geometry when projecting the radiated power.

In addition to the photon loading, a contribution due to CXN should also be included (Section 1), but this is not assessed here and requires full 3D modelling of edge recycling, including the shaped first wall. Estimates based on unpublished 2D plasma code simulations performed at the ITER Organization indicate peak loads of ~0.025 MWm^{-2} at the outboard midplane location for the same broad (inter-ELM) SOL particle flux density profiles as those assumed here. These estimates do need to be refined by 3D plasma boundary simulations and can also be influenced by local gas puffing in the antenna vicinity [3], which is planned for implementation in the ITER baseline as a promising tool to improve coupling of RF power to the plasma.
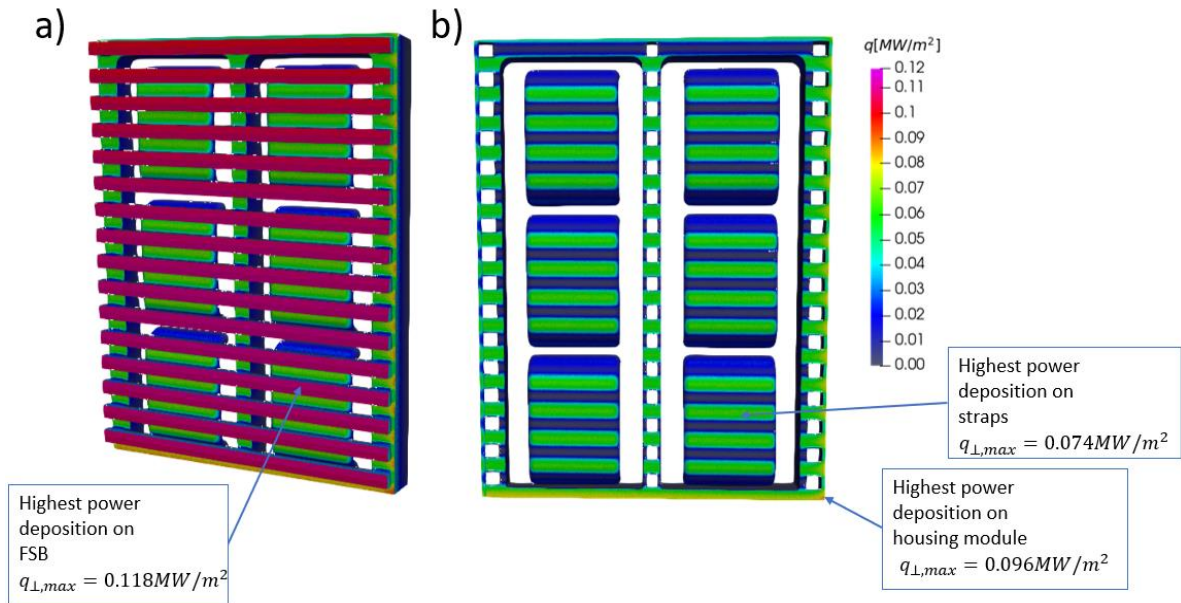
Figure 7: Radiative heat loads on the antenna for the worst case with W rotation (see Fig. 4). a) FSBs b) antenna straps and housing module. The loads are computed for the baseline, unshifted equilibrium (they are essentially unaffected by the outboard separatrix shift).

4. Conclusions

This paper has presented a case study for the maximum stationary power loading to be expected due to plasma thermal and radiative components on the front end structures (namely the Faraday screen) of the ITER ICRH antennas during Q = 10 burning plasma operation. The computed values are valuable input to the antenna design activities, which, at the time of writing, are just entering the final phase.

Plasma thermal loading is assessed on the basis of an H-mode, mitigated ELM scenario, with worst case radial profiles of stationary, inter-ELM heat fluxes and an averaged ELM heat flux profile derived from a model of ELM filament parallel transport losses. Both have been deployed in previous design studies for the ITER beryllium first wall panel power handling. The antenna and associated first wall heat loads are derived in full 3D using the sophisticated field line tracing environment, SMITER, which maps the specified SOL radial heat flux profiles onto the antenna and shaped first wall panels, numerically meshed from CAD model inputs. Three-dimensional perturbations of the magnetic field lines, e.g. caused by currents in ELM coils have not been taken into account.

Importantly, the antenna (and first wall) loads have been derived for a series of magnetic equilibria in which, starting from the baseline burning plasma magnetic geometry, the outer midplane separatrix is moved towards the antenna in a series of steps to investigate the antenna loading as the plasma-wall gaps decrease. Such plasma displacements are one option by which to improve the coupling of RF power to the plasma, or to operate the antenna at lower RF voltage, if this proves to be necessary or beneficial during real operation.

In addition to the thermal plasma load, the antenna (and the first wall) also receive photon heat loads from core plasma radiative losses. These are simulated here using the Raysect ray propagation software package, taking as radiative source realistic worst case core radiation distributions from integrated model simulations of the burning plasma, including tungsten impurity and possible poloidal asymmetries in this radiation caused by neoclassical transport in the presence of plasma rotation. Heating of antenna structures due to charge-exchange neutral loading (expected to be low compared to the photon loading) and volumetric neutron deposition are not considered here.

The analysis shows that no thermal plasma antenna loading is to be expected for the baseline (unshifted) separatrix position since first wall panels on the shield blocks either side of the antenna location will prevent magnetic field lines accessing antenna structures. As the outboard separatrix is moved progressively closer to the antenna, field line penetration begins to occur and surface heat loads appear on the Be armoured antenna Faraday screen bars. Peak values of these loads of ~2.1 MWm^{-2} are found for the largest radial separatrix displacements (~10 cm) studied here, at which point the primary separatrix is only ~10 cm from the outboard first wall at the outboard midplane. Whilst more antenna design activities are required to conclude if this is acceptable, such plasma displacements are shown to be marginal for the first wall panels neighbouring the antenna.

Regarding photon loading, this has been assessed to high degree of fidelity with the modelling here, but the maximum loads (~0.12 MWm^{-2}) are small in comparison to the peak thermal plasma contribution. The slightly lower heat loads found on the strap surfaces, inaccessible to plasma fluxes, are nevertheless important to account for in the comprehensive thermal and mechanical load case analyses that are mandatory to validate the final design.

Acknowledgements

References
[1] L. Kos et al., Fus. Eng. Des. **146** (2019) 1796

[2] A. Meakins and M. Carr (2017), "Raysect Python raytracing package," version v0.4.0, Zenodo, http://doi.org/10.5281/zenodo.1205064

[3] W. Zhang et al., Nuclear Materials and Energy **19** (2019) 364

[4] R.A. Pitts et al., 2011 J. Nucl. Mater. **415** 1

[5] A. Loarte et al., Nucl. Fusion **54** (2014) 033007

[6] H. Anand et al., Nucl. Fusion **60** (2020) 036011

[7] M. Kočan et al., J. Nucl. Mater **463**, 2015, Pages 709-713, ISSN 0022-3115

[8] W. Fundamenski et al., Plasma Phys. Control. Fusion **48** (2006) 109

[9] G.T.A. Huijsmans and A. Loarte, Nucl. Fusion **53** (2013) 123023

[10] A. R. Polevoi A.R. et al., Nucl. Fusion **58** (2018) 056020

[11] M. Romanelli, et al., Plasma and Fusion Research **9** (2014) 34030233

[12] F. Köchl et al., Plasma Phys. Control. Fusion **60** (2018) 074008

[13] M. Moscheni et al., submitted to PSI 2020

[14] R. Mitteau et al., J. Nucl. Mater. **463** (2015) 411